Universiteit
Leiden
The Netherlands

On the geometry of demixing: A study of lipid phase separation on curved surfaces

Rinaldin, M.

Citation
Rinaldin, M. (2019, November 7). *On the geometry of demixing: A study of lipid phase separation on curved surfaces*. *Casimir PhD Series*. Retrieved from https://hdl.handle.net/1887/80202

Version:	Publisher's Version
License:	Licence agreement concerning inclusion of doctoral thesis in the Institutional Repository of the University of Leiden
Downloaded from:	https://hdl.handle.net/1887/80202

Note: To cite this publication please use the final published version (if applicable).

Cover Page

Universiteit Leiden

The handle http://hdl.handle.net/1887/80202 holds various files of this Leiden University dissertation.

Author: Rinaldin, M.
Title: On the geometry of demixing: A study of lipid phase separation on curved surfaces
Issue Date: 2019-11-07

CHAPTER 4

ON THE MECHANICS AND THERMODYNAMICS OF PHASE SEPARATION IN CURVED SPACE

Inspired by the experimental results on multicomponent lipid membranes supported by colloidal scaffolds, we report a theoretical investigation on the equilibrium configurations of binary mixtures on curved substrates. First, starting from the Jülicher and Lipowsky generalisation of the Canham-Helfrich free energy of multicomponent membranes, we derive several exact relations governing the structure and stability of an interface separating two lipid phases on curved substrates. Second, we build a curved-space generalisation of the two-dimensional Ising lattice gas model. The resulting free energy landscape admits, as stable equilibria, states with dominant lipid sorting. Our work sheds light on the interaction mechanism between local membrane shape and chemical composition. Furthermore, it provides a robust framework for interpreting results from experiments on supported lipid bilayers.

This chapter is the result of a collaboration with Piermarco Fonda who developed and performed the analytical calculations and numerical simulations presented here. The text is based on:

P. Fonda, **M. Rinaldin**, D. J. Kraft, and L. Giomi, Interface geometry of binary mixtures on curved substrates, *Phys. Rev. E* **98**, 032801 (2018).

P. Fonda, **M. Rinaldin**, D. J. Kraft, and L. Giomi, Thermodynamic equilibrium of binary mixtures on curved surfaces, *Phys. Rev. E*, **100**, 032604 (2019).

4.1 Introduction

Motivated by experiments with phase-separated colloid supported lipid bilayers (CSLBs) we present here a theoretical study of liquid-liquid phase separation (LLPS) in lipid membranes of fixed curved geometry. Information on the experimental system can be found in Chapter 3 to which this chapter directly follows.

4.2 On the mechanics of phase separation on curved surfaces

LLPS in artificial lipid bilayers has been widely investigated[147;148] and the interplay between membrane shape, domain formation, and lateral displacement has been studied in several experimental set-ups[4;6;18] which include CSLBs reported in this thesis. The coexistence of two-dimensional phases implies that a stable linear interface must exist, dividing the membrane into different domains. As in every phase coexistence, this interface has a non-vanishing line tension[149].

Alongside experiments, a comparable effort has been done on the theoretical side to construct models able to account for the experimental observation. The various approaches can be roughly divided into two main classes. The first one, pioneered by the works of Leibler and Andelman[57;58], focuses on the statistical nature of phase separation, treating the membrane as a set of concentration fields interacting with the environment. These fields and their associated thermodynamic potentials are, ideally, emergent mean-field descriptions of the underlying coarse molecular structure. In contrast, the second approach is geometrical and treats lipid domains as regions on a two-dimensional surface bounded by one-dimensional interfaces. This view falls within the fluid-mosaic model[150] and is a natural generalisation of the Canham-Helfrich approach[59;60] to multi-component membranes, first introduced by Jülicher, Lipowsky and Seifert[62–64].

Here, we follow the latter geometric approach and model phase domains as perfectly thin two-dimensional surfaces. Motivated by the experimental results of Chapter 3, we restrict our analysis to the case of membranes with fixed geometry, such that the only degree of freedom of the system is the position of the interface: the free energy is a functional of embedded curves. This assumption is appropriate for membranes which are attached to some support and are not free to change their shape.

The central focus of this section is the shape of the interface and how it is influenced by the underlying geometry of the membrane. Interfacial lines are obtained as solutions of an interface equation and need to be stable against fluctuations. These requirements are significantly more intricate than interface problems in homogeneous and isotropic environments. For instance, coexisting phases in three-dimensional Euclidean space tend to minimise their contact area and the resulting interface is either planar or spherical, in case of non-zero Laplace pressure. Similarly, on a two-dimensional flat plane, interfaces are either straight lines or circles.

As we will demonstrate in the following subsections, this scenario changes dramatically for non-flat membranes. Spatial curvature introduces three essential features that are not present on flat substrates. First, curves on surfaces can be simultaneously curved and

length-minimising (*i.e.* geodesic). As a consequence, stable closed interfaces can exist on a curved substrate even for vanishing Laplace pressure. Second, as different lipid phases generally possess different elastic moduli (with the liquid-disordered, LD, phase being more compliant to bending than the liquid-ordered, LO, phase), non-uniform substrate curvature can drive the segregation of lipid domains, with the stiffer phase preferentially located in regions of low curvature at the expenses of the softer phase (i.e. geometric pinning). Third, the surface curvature directly influences the stability of interfaces. In particular, interfaces located in regions of negative Gaussian curvature (*i.e.* saddle-like) generally tend to be more stable, as any deviation from their original shape inevitably produces an increase in length.

This section is organised as follow. We will first remind the basic assumptions of our theoretical model and the energy functional that depends only on the interface that we introduced in the previous chapter. We will show how closed interfaces are stabilised by negative curvature and how curvature affects phase separation locally. Finally, we will investigate the global effect of curvature on spherical and axis-symmetric surfaces.

4.2.1 The interface equation. We model a phase-separated lipid membrane as a two-dimensional elastic sheet with closed surface S and interface L, as described in the Introduction in Section 1.4.2 and in Chapter 3 in Section 3.4. We label the LO and LD lipid phases with $\{+,-\}$, respectively, and we denote with φ the area fraction occupied by the "$-$" phase.

Since S does not change with time, an equilibrium state can be described by the position of the interface L. As a consequence, the minima of the Canham-Helfrich free energy F (Equation 1.15) can be obtained by finding lines on the surface S which satisfy the constraints imposed by the shape and the material properties of the membrane. Analytically, this can be done by calculating the first variation of the Canham-Helfrich free energy F with respect to the position of the interface. In this way, we derive an equation for the equilibrium condition for a phase-separated membrane:

$$\sigma\kappa_g = \Delta k\, H^2 + \Delta\bar{k}\, K + \Delta\lambda\,, \tag{4.1}$$

where κ_g is the geodesic curvature of L and σ is the interfacial line tension between the two lipid phases. The quantities H and K are the mean and Gaussian curvature calculated along the interface L, respectively. $\Delta k = k_+ - k_-$ and $\Delta\bar{k} = \bar{k}_+ - \bar{k}_-$ are the difference in bending rigidity and splay modulus of the two phases, respectively. $\Delta\lambda = \lambda_+ - \lambda_-$ is the difference between the Lagrange multipliers. In Chapter 3, we showed how this equation can be considered as the curved-space analogue of the Young-Laplace law.

By calculating the second variation of Equation 1.15 with respect to the position of the interface, we can obtain the stability condition for the interface under an arbitrary perturbation:

$$\sigma\left(K + \kappa_g^2\right) + \Delta k\, \nabla_{\boldsymbol{N}} H^2 + \Delta\bar{k}\, \nabla_{\boldsymbol{N}} K < 0\,, \tag{4.2}$$

where $\nabla_{\boldsymbol{N}}$ is the surface-covariant directional derivative along the tangent-normal of L (the vector $\boldsymbol{N}$ is shown in Figure 4.1). To reduce the number of independent parameters

in 4.1, we introduce the dimensionless numbers:

$$\eta_k = \frac{\Delta k}{\sigma l} \,, \qquad \eta_{\bar{k}} = \frac{\Delta \bar{k}}{\sigma l} \,, \tag{4.3}$$

which express the relative contribution of bending and interfacial tension to the total energy. The quantity l denotes the characteristic length of the system and can be chosen, on a case-by-case basis, depending on the symmetry of the surface. For instance, in the case of a sphere l is the radius of the sphere.

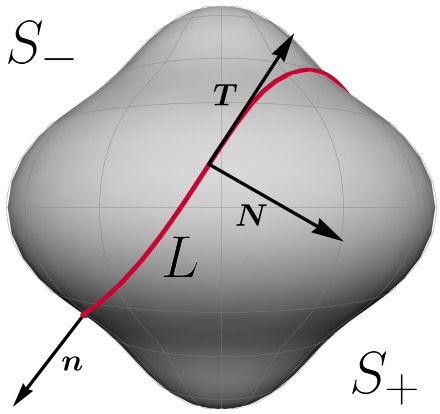

Figure 4.1: Spinning top shaped membrane partitions into two connected domains $\mathbf{S}_+$ and $\mathbf{S}_-$, separated by the interface L. We show the normal and the tangent vectors **N** and **T**, along with the normal to the surface **n**.

These numbers are the only parameters necessary to determine the interface position, if and only if the shape of S is kept fixed. Conversely, when comparing different shapes one should keep in mind that the geometry enters into the problem locally, thus η_k and $\eta_{\bar{k}}$ only give a general indication of whether the force balance at the interface is dominated by bending or tension. They are not sufficient by themselves to determine the shape of the interface or to predict whether there will be only two or multiple domains.

4.2.2 Geodesic and constant geodesic curvature interfaces. Equation 4.1 reduces the physical problem of identifying the interface between two lipid phases to the geometrical problem of finding curves embedded on surfaces whose geodesic curvature depends directly on both intrinsic and extrinsic properties of the immersion. This is in general a challenging task, not only because the membrane geometry influences the local behaviour of the interface, but also because for a curve to be an admissible interface it needs to be closed and simple (*i.e.* without self-intersections). These are global properties and need to be considered with care.

As a starting point, let us assume that the local membrane curvature does not influence the interface position, so that $\eta_k = \eta_{\bar{k}} = 0$. Furthermore let us consider the case in which the total area occupied by the lipid phases is not conserved, hence $\Delta\lambda = 0$. In practice, this happens if the membrane is in contact with a lipid reservoir. Then, Equation 4.1 becomes simply:

$$\kappa_g = 0 \,, \tag{4.4}$$

telling us that L is a closed geodesic of S. The latter is a curved-space generalisation of the intuitive property of interfaces, which pay a fixed energetic cost per unit length, to minimise their extension (similarly, two-dimensional interfaces at equilibrium are minimal surfaces with $H = 0$).

On a flat substrate, the only solutions of Equation 4.4 are straight lines. A compact closed surface, on the other hand, allows for richer structures and in particular it admits simple closed geodesics, *i.e.* geodesic lines of finite length which do not self-intersect. For example, on a sphere every great circle has $\kappa_g = 0$ and for every point on the surface there are infinite simple closed geodesics. However, for less symmetric surfaces this might not necessarily be true. This implies that regions of the surface that do not admit closed geodesics cannot host an interface such as the one obtained under the current assumptions. Nonetheless, it is known that every genus zero surface admits at least three simple closed geodesics[151]. The stability of geodesic interfaces can be easily assessed by taking $\eta_k = \eta_{\bar{k}} = 0$ and setting $\kappa_g = 0$ in Equation 4.2. This yields:

$$K < 0 \,, \tag{4.5}$$

thus curves lying in saddle-like regions are inherently stable. This can be intuitively understood by looking at the blue curve in Figure 4.2. Moving the interface away from the saddle would inevitably result into an increase of its total length. Conversely, no geodesic lying on regions with positive curvature can represent a stable interface, as its length could always be shortened by a small displacement, as illustrated by the black curve in Figure 4.2. In particular, no geodesic of the sphere is stable for non-fixed area fraction φ.

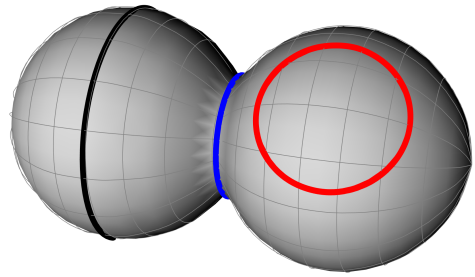

Figure 4.2: Constant geodesic curvature (CGC) curves on a generic surface. The black line is an unstable closed geodesic: its length can be easily shortened by a shift in any direction. Conversely, the blue line is a stable geodesic, lying along a region of negative K, and whose length can only be increased by fluctuations. The red curve is a closed CGC. Since this surface is axis-symmetric, meridians and parallels are also principal directions. This dumbbell-shaped surface was taken from the experimental images in Chapter 3 and is also used to construct the phase diagram of Figure 4.5.

Next, let us consider the case where the two phases still have identical bending rigidities but their area fractions are kept fixed. Equation 4.1 yields a curved background analogue of the Young-Laplace equation, namely:

$$\kappa_g = \frac{\Delta\lambda}{\sigma} \,. \tag{4.6}$$

Thus, if φ is fixed but there is no difference in the elastic moduli, the interface consists of a curve of constant geodesic curvature (CGC), such as the red curve in Figure 4.2.

We emphasise that $\Delta\lambda$ is determined solely by the area constraint and, if L consists of multiple disconnected curves, it can take on different values in each of them. This allows the existence of multiple domains bounded by interfaces of constant geodesic curvature. Regardless of their stability, however, configurations featuring multiple domains tend to be metastable as they usually are local minima of the free energy in the absence of a direct coupling with curvature.

We stress that the stability condition for fixed φ is not given by Equation 4.2, because only variations that do not change the relative area fractions are allowed. Unfortunately, the explicit expression of the second variation is not particularly illuminating unless the geometry of S is made explicit. Therefore we leave further considerations to when we discuss specific examples.

4.2.3 Local effects. In this section, we explore how the mean and Gaussian curvature locally affect the shape of the interface depending on $\Delta\lambda$ (the difference of the two Lagrange multipliers), σ (the line tension), and η_k and $\eta_{\bar{k}}$ (the dimensionless parameters that express the relative contribution of bending and interfacial tension to the total energy). We consider a generic surface and we locally approximate it as a quadric, by constructing a Cartesian frame whose origin is a point on the surface, the x and y axes correspond to the principal directions, and z corresponds to the surface normal $\mathbf{n}$.

In a small neighbourhood around the origin, the surface can be approximated with a local Monge patch as:

$$z = \frac{1}{2}(\kappa_1 x^2 + \kappa_2 y^2)\,, \tag{4.7}$$

where κ_1 and κ_2 are the two principal curvatures at the origin. The interface can be described with a pair of functions of the arc-length s: $\{x, y\} = \{x(s), y(s)\}$. We parametrise the unit tangent along the interface as $\boldsymbol{T} = \cos\theta\,\hat{\boldsymbol{x}} + \sin\theta\,\hat{\boldsymbol{y}}$, where $\hat{\boldsymbol{x}}$ and $\hat{\boldsymbol{y}}$ are unit vectors in the $x-$ and $y-$direction and $\theta = \theta(s)$ is the angle between $\boldsymbol{T}$ and $\hat{\boldsymbol{x}}$. We choose s such that $x(0) = y(0) = 0$ and we fix $\theta(0) = \theta_0$ to be the direction of $\boldsymbol{T}$ at the origin. We use a dot to indicate differentiation with respect to the arc-length, namely: $\dot{(\cdots)} = \frac{d(\cdots)}{ds}$.

Substituting Equation 4.7 into Equation 4.1 and expanding for small s, we find:

$$\kappa_g = \dot{\theta}_0 + s\left[\ddot{\theta}_0 - \kappa_{n0}\tau_{g0}\right] + O(s^2)\,, \tag{4.8}$$

where κ_n and τ_g are the normal curvature and the geodesic torsion of L, respectively. The 0 subscript denotes the value at the origin. Similarly, we can evaluate and expand up to $O(s^2)$ the surface curvatures along L:

$$H^2 = H_0^2 + O(s^2), \tag{4.9a}$$

$$K = K_0 + O(s^2). \tag{4.9b}$$

The lack of linear terms in s in Equations 4.9 reflects that the parametrisation given in Equation 4.7 approximates S at second order in both x and y. Substituting Equations 4.8 and 4.9 into 4.1, we can solve the resulting equation order by order in powers of s. At

order zero, we find that Equation 4.1 constrains the value of $\dot{\theta}_0$. Note that the quantity $r_0 = 1/\dot{\theta}_0$ is the radius of curvature of the interface on the tangent plane at $s = 0$ (*i.e.* the radius of the osculating circle on the plane identified by the vectors $\mathbf{T}$ and $\mathbf{N}$). The interface equation fixes this radius to:

$$r_0 = \frac{1}{l(\eta_k H_0^2 + \eta_{\bar{k}} K_0) + \frac{\Delta\lambda}{\sigma}}\,, \tag{4.10}$$

where l is the length scale used in the definitions Equation 4.3. We observe that even in the case of non-fixed area fraction, for which we have $\Delta\lambda = 0$, the situation is significantly different with respect to the flat case. As a consequence of the substrate local curvature, the interface deviates from a geodesic (for which $r_0 \to \infty$), becoming more and more curved the larger is the difference in stiffness between the two lipid phases.

At order $O(s)$, we find the condition $\ddot{\theta}_0 = \kappa_{n0}\tau_{g0}$ which does not depend on bending rigidities: it is the same for a geodesic, and states that the rate of change of r_0 along L depends only on the direction of $\boldsymbol{T}$. In fact, it vanishes for asymptotic lines (curves with vanishing normal curvature) and for lines of curvature (curves with vanishing geodesic torsion). Higher order contributions are less illuminating.

Figure 4.3 shows the interfaces resulting from a numerical solution of Equation 4.1 for the quadric surface used with different principal curvatures and various material parameters. As expected, while $\Delta\lambda$ has roughly the same effect on L independently on the surface curvature (see the first row of the figure), a non-zero curvature coupling produces very different effects depending on the local bending of S.

4.2.4 Global effects. While in the previous section we analysed the effect of inhomogeneous local curvature for open surfaces, here we study the global effects of the interplay between the shape, material properties, and area fraction of the membrane of specific closed surfaces. We report the result for spheres and axis-symmetric geometries, two shapes which are at the same time simple to describe from a mathematical point of view and interesting because used in the experiments.

The sphere

The sphere is the most simple closed surface and common vesicle shape found in nature, being the absolute minimum of both the area and the bending energy. The mean and Gaussian curvatures are constant throughout the surface and equal to:

$$H^2 = K = 1/R^2, \tag{4.11}$$

with R the sphere radius.
In this way, the Canham-Helfrich free energy in Equation 1.15 becomes:

$$F = \sum_{\alpha=\pm} \lambda'_\alpha \int_{S_\alpha} \mathrm{d}A + \sigma \int_L \mathrm{d}s\,, \tag{4.12}$$

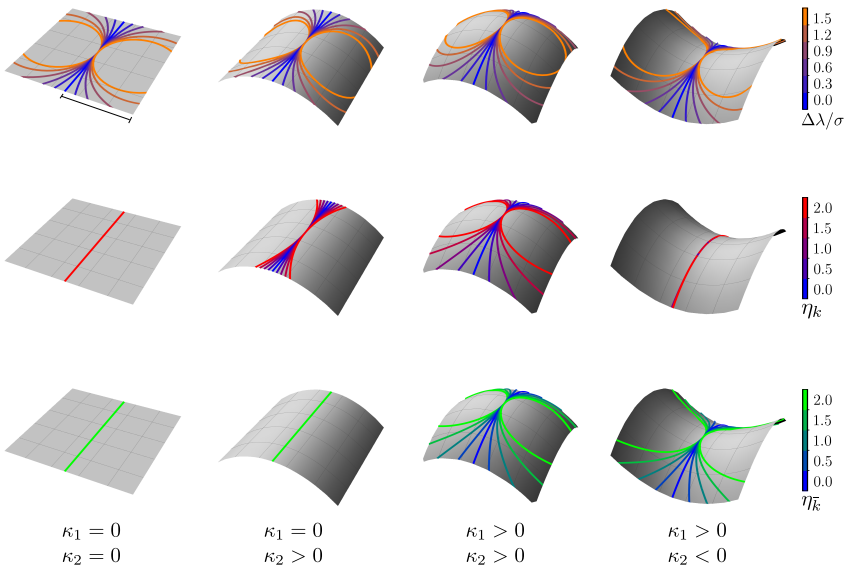

Figure 4.3: Local effects of surface and material properties on the interface. The four columns correspond from left to right to a flat plane, a parabolic cylinder, a symmetric paraboloid, and a hyperboloid. The three rows show the effect of the variation of the three different open parameters in the system. Different curve colours correspond to different values of the coupling constants which are shown on the right.

where $\lambda'_\alpha = \lambda_\alpha + (k_\alpha + \bar{k}_\alpha)/R^2$ is a constant. The interface equation then reduces to:

$$\kappa_g = \frac{\Delta\lambda'}{\sigma}, \tag{4.13}$$

with $\Delta\lambda'$ replacing $\Delta\lambda$. This corresponds to circles of constant geodesic curvature:

$$\kappa_g = \frac{\cot\psi}{R}\,, \tag{4.14}$$

where ψ is the usual azimuthal angle in spherical coordinates. The fractional area occupied by such a domain is:

$$\varphi = \frac{1-\cos\psi}{2}\,. \tag{4.15}$$

Consistent with our convention on the sign of curvatures, we choose $\psi < \pi/2$ for a soft phase domain with $\varphi < 1/2$ and $\kappa_g > 0$. If the area fractions are not conserved ($\lambda_\alpha = 0$), the interface equation admits as solution CGC lines with azimuthal angle:

$$\cot\psi = \eta_k + \eta_{\bar{k}}\,, \tag{4.16}$$

where we have set $l = R$ in the definitions of 4.3. These interfaces are, however, always unstable, thus, for non-conserved area fractions, spherical vesicles cannot support interfaces. In practice, this implies that a multicomponent CSLB allowed to exchange lipids with the environment will eventually expel the stiffer phase. We observed this phenomenon in experiments of SLBs on substrate topographically patterned with colloidal particles in which the membrane of the spherical CSLBs is in contact with a reservoir. We report these experimental results in Chapter 5, Section 5.3.2.

For conserved area fractions, on the other hand, it can be demonstrated that CGC lines become stable, as the second variation of the free energy is always non-negative. Although CGC lines are always stable on the sphere, configurations featuring multiple domains are inevitably local minima of the free energy, whereas the configuration consisting of a single hard and a single soft domain is the global minimum. These considerations evidently do not apply to giant unilamellar vesicles, where multiple circular domains are often observed[152]. This can be ascribed to the budding of phase domains[12], where small domains locally deform the membrane and are stabilised from fusing by the local curvature that they create around them.

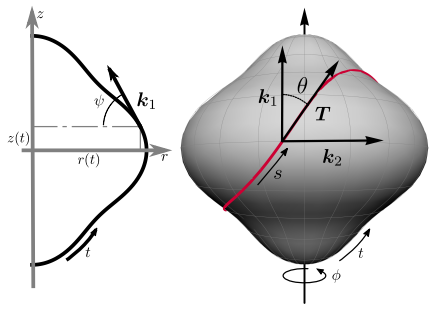

Figure 4.4: Parametrisation of an axis-symmetric surface. On the left, we show the radial profile $\{r(t), z(t)\}$ as a function of t, the arc-length parameter of the profile. The full surface is obtained by rotations along the z axis parametrised by the angle ϕ, as in Equation 4.17. We define $\psi = \psi(t)$ to be the angle between $\boldsymbol{k}_1$, the meridian principal direction, and the horizontal plane. On the right, we show how how the curve L in S is parametrised in its own arc length s; its unit tangent vector $\boldsymbol{T}$ makes an angle $\theta = \theta(s)$ with $\boldsymbol{k}_1$.

4.2.5 Axis-symmetric surfaces. To appreciate the effect of the underlying geometry, surfaces with non-uniform curvature must be considered. As we described in Chapter 3, dumbbell-shaped surfaces are interesting scaffolds for the membrane because on the one hand they are simple to describe because they are symmetric under rotation, and on the other hand they present inhomogeneous curvature. In this section, we first discuss the case of axis-symmetric surfaces in general and then, we study the specific case of dumbbell-shaped surfaces.

Rotationally invariant surfaces are completely characterised by their radial profile, and as a consequence of choosing $\hat{\boldsymbol{z}}$ as symmetry axis, arbitrary axis-symmetric surfaces can be parametrised as:

$$\boldsymbol{r}(t, \phi) = \{r(t)\cos\phi, r(t)\sin\phi, z(t)\} \ , \tag{4.17}$$

where t is the arc-length parameter of the cross-section and $\phi \in [0, 2\pi]$ is the polar angle on the $xy-$plane (Figure 4.4). The mean and Gaussian curvatures are then given by:

$$H = -\frac{1}{2}\frac{d\psi}{dt} - \frac{\sin\psi}{2r}\,, \qquad K = \frac{\sin\psi}{r}\,\frac{d\psi}{dt}\,, \tag{4.18}$$

where $\psi = \psi(t) = \arctan(dz/dt)/(dr/dt)$ is the angle between the meridian direction $\boldsymbol{k}_1$ and the constant $z-$plane, as shown in Figure 4.4.

When evaluated along L, both curvatures are functions of the arc-length coordinate s. The principal directions coincide with parallels and meridians. The latter, in particular, are also geodesic (they are the shortest path between points with the same angular coordinate ϕ), hence have vanishing geodesic curvature. On the other hand, the parallels have in general non-zero geodesic curvature:

$$\kappa_g(\boldsymbol{k}_2) = \frac{\cos\psi}{r}\,. \tag{4.19}$$

More generally, a curve L on an axis-symmetric surface can be parametrised by a pair of functions $\{t(s), \phi(s)\}$ and its geodesic curvature can be expressed in the form:

$$\kappa_g = \dot{\theta} + \frac{\sin\theta\cos\psi}{r} = \frac{1}{r}\frac{d}{dt}\left(r\sin\theta\right)\,, \tag{4.20}$$

where $\theta = \theta(s)$ is the angle between the tangent vector of L and the local meridian, so that $\boldsymbol{T} = \dot{\boldsymbol{r}} = \cos\theta\,\boldsymbol{k}_1 + \sin\theta\,\boldsymbol{k}_2$. Equation 4.20 implies the so called Clairaut relation, according to which geodesics with $\theta \neq \pi/2$ on axis-symmetric surfaces satisfy:

$$r\sin\theta = \text{const}\,. \tag{4.21}$$

In particular, meridians, whose tangent vector is parallel to $\boldsymbol{k}_1$, have $\theta = 0$ and are thus geodesics. Using Equations 4.18 and 4.20, the interface equation can be cast in the form:

$$\frac{1}{r}\frac{d}{dt}\left[r\sin\theta + \left(\frac{\Delta\bar{k}}{\sigma} + \frac{\Delta k}{2\sigma}\right)\cos\psi\right] = \frac{\Delta k}{4\sigma}\left[\left(\frac{d\psi}{dt}\right)^2 + \frac{\sin^2\psi}{r^2}\right] + \frac{\Delta\lambda}{\sigma}\,. \tag{4.22}$$

This interface equation is integrable because it can always be expressed in the generic form:

$$\frac{1}{r}\frac{d}{dt}\left[r\sin\theta + f(t)\right] = 0\,, \tag{4.23}$$

with a properly chosen $f(t)$. The quantity between brackets is a constant of motion whose conservation is a direct consequence of the rotational invariance of the surface.

For generic couplings η_k, $\eta_{\bar{k}}$, and $\Delta\lambda$ finding such $f(t)$ amounts to finding the

$t-$primitive function of the right-hand side of Equation 4.22, which is not always possible analytically and moreover not particularly useful. However, if $\Delta\lambda = 0$ and there is no coupling with mean curvature (*i.e.* $\Delta k = 0$), we find the relation:

$$r \sin\theta + \frac{\Delta\bar{k}}{\sigma} \cos\psi = \text{const}, \tag{4.24}$$

which is true for any $r(t)$. The value of the constant is fixed by boundary conditions. In general, for any given substrate geometry, there is a plethora of possible solutions to the interface equation.

To gain insight into the physical mechanisms underlying geometric pinning in axis-symmetric surfaces, we make the further assumption that, like the substrate, the interface is also rotationally invariant. Then, for conserved area fractions, every parallel is a solution of the interface equation for a specific φ value, regardless of the values of η_k and $\eta_{\bar{k}}$. The problem thus reduces to finding a configuration of domains which minimises the free energy.

Intuitively, for small η_k and $\eta_{\bar{k}}$ the force balance is dominated by line tension. Thus, the system partitions into two domains separated by a single interface, whose position is trivially determined by the area fraction. Upon increasing η_k and $\eta_{\bar{k}}$, on the other hand, configurations featuring multiple domains might become energetically favoured. We stress that the number of domains alone is not necessarily a good indicator of the strength of geometric pinning, as complex substrate geometries can allow for stable equilibria with multiple domains even when $\eta_k = \eta_{\bar{k}} = 0$. In this respect, curved and flat substrates are dramatically different from each other, as on flat substrates interfaces are always circular (or straight as a limiting case).

Dumbbell-shaped membranes

As a concrete example, in Figure 4.5 we show the phase diagram of a dumbbell-shaped binary vesicle. In the left panel of Figure 4.5, we set $\eta_{\bar{k}} = 0$ while varying the area fraction φ and η_k, while in the right panel we vary $\eta_{\bar{k}}$ and φ and keep $\eta_k = 0$. We compared the total energy of different types of configurations, here labelled I, $II_{\pm}$, and $III_{\pm}$. In the insets, the "$+$" domains are coloured in green, and the "$-$" domains in magenta. Type I is the configuration consisting of only two domains, separated by a single interface. Types $II_{\pm}$ and $III_{\pm}$ consist of three domains and two interfaces. Configurations $II_{\pm}$ have always one interface lying along the dumbbell neck (where the interface is shortest), while the second interface varies according to the value of φ. Configurations $III_{\pm}$ instead, have two symmetrical interfaces at the same distance from the neck region.

As expected, for $\eta_k = 0$ the only stable configuration consists of two domains separated by a single interface (type I). However for $\eta_k > 0$ we observe that three-domain configurations can become favourable when $\varphi < 0.5$. Similarly, for $\eta_k < 0$ we found that three domains become favourable for $\varphi > 0.5$. This symmetry of the phase diagram is a direct consequence of the fact that the free energy in Equation 1.15, is invariant under the transformation $\eta_k \to -\eta_k$ and $\varphi \to 1 - \varphi$. The right panel shows that the situation for non-zero $\eta_{\bar{k}}$ is reversed: in order for the configuration III_+ to become energetically favourable, we need to have $\eta_{\bar{k}} < 0$.

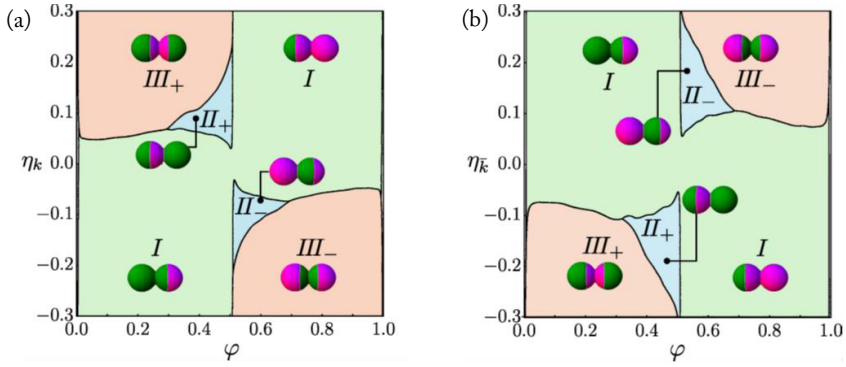

Figure 4.5: Phase diagrams of the dumbbell-shaped membrane for varying area fraction, φ. (a) Effect of $\eta_k = \frac{\Delta k}{\sigma l}$ while keeping $\eta_{\bar{k}} = \frac{\Delta \bar{k}}{\sigma l} = 0$. **(b)** Effect of $\eta_{\bar{k}}$ while keeping $\eta_k = 0$. In both panels, different colours correspond to different minimal energy configurations: type I (light green) consist of two domains and one interface; types $II_\pm$ (light blue) and types $III_\pm$ (light red) have two interfaces and three domains. In the insets, hard and soft phases are respectively depicted in green and magenta. All interfaces are constant geodesic curvature parallers. We set $l = \sqrt{A_S}$.

4.3 On the thermodynamics of phase separation on curved surfaces

Until now, we presented an analytical model to study the effect of curvature on the spatial arrangement of coexisting lipid domains on curved substrates. However, there is evidence that curvature also affects lipid sorting, *i.e.* the relative lipid partitioning into ordered and disordered domains[15].

It was shown *in vivo* that lipid sorting occurs in the formation of highly curved vesicles during intracellular transport. In particular, a study on vesicles in the Golgi network showed that sphingolipids are depleted from retrograde carriers and enriched in anterograde ones[15;153;154]. Experiments *in vitro* have also shown that curvature affects lipid sorting[6–8]. In a set-up consisting of a vesicle in which a tube was pulled out and stabilised with optical tweezers or micro-pipette aspiration, it was found that the relative amount of lipids in the vesicle and the tubes depends on the vicinity to the critical point and, more importantly, the value of curvature of the tube[6–8]. In Chapter 3, we have also reported experimental evidence of lipid sorting induced by curvature. We have termed this phenomenon antimixing because the concentration of the sub-domains are located on antipodes of a local miscibility gap. We remind that antimixing is a thermodynamic state which can be induced by any location-dependent coupling of the mixture concentration, and becomes relevant only in closed systems.

Here, we focus on describing the thermodynamics in the latter system, CSLBs, since it is at the same time closed (*i.e* there is no exchange of lipids with the surroundings) and has prescribed shape. We stress, nonetheless, that the results of the present work apply, in principle, to any generic two-dimensional liquid mixture confined on a curved substrate.

CSLBs have typical size of a few micrometres , whereas a single lipid molecule occupies an area on the membrane of order $\sim$ 1 nm^2 [155]: therefore, the number of constituents is approximately in the millions. With such a high number of molecules, it is natural to describe the membrane as a single smooth surface where the local composition is a continuous space-dependent field. A satisfactory physical description can be attained by a coarse-grained two-dimensional scalar field theory, with the fields representing the concentration of the various molecule types. For incompressible liquids, an n-component mixture is described by $n-1$ fields.

Much of this section will focus on the ability of a single scalar field, ϕ, to describe the curvature-composition interactions. Despite being appropriate for binary systems only, a single scalar degree of freedom can capture, at least qualitatively, the effect of geometry on the structure of the free energy landscape and the resulting phase behaviour. Furthermore, focusing on a single field has numerous advantages, as it roots in the classical theory of phase separations and was first used to model the interaction between curvature and lipid lateral organization by Markin [156] and Leibler [57]. In the latter work, the interplay between the membrane chemical composition and geometry was modelled in terms as a concentration-dependent spontaneous mean curvature, leading to a linear coupling in the effective free energy, analogous to that between an order parameter and an external ordering field. Such coupling breaks the reflection symmetry along the membrane mid-surface, since the mean curvature is sensitive to the surface orientation.

This type of interaction was adopted by many subsequent works [58;157–163], whereas others [164–166] also considered linear couplings with the squared mean curvature, which is better suited to describe symmetric bilayers. Conversely, other works did not introduce any interaction terms but instead studied the effects of a non-trivial intrinsic geometry [167–169]. Explicit intrinsic couplings were considered in Paillusson *et al.* [170], with a direct coupling to the Gaussian curvature, and by Adkins *et al.* [171], where the notion of spontaneous geodesic curvature was introduced. Note that, because of the Gauss-Bonnet theorem, a direct coupling between the Gaussian curvature and the concentration is irrelevant for chemically homogeneous membranes, and likely, for this reason, it has often been disregarded. Couplings quadratic and cubic in ϕ were considered in other works [172–179] and appear to be the most popular choices within the mathematics-oriented literature.

There is no general consensus on how to choose neither the type nor the functional form of the couplings between the shape and the concentration. Although linear terms are the natural choice from a field-theoretic point of view, it is not clear how model-specific the results will be, and thus it is hard to assess their general validity. Furthermore, most of the cited works focus on the local and dynamical effect of given couplings in an open setting. However, vesicle-shaped objects are inherently constrained systems, being topologically spherical and with no relevant exchange with the surrounding environment: the total number of molecules is an externally fixed parameter. For these reasons, we try to have a more systematic approach and explore all the possible equilibrium configurations of closed two-dimensional systems. For the sake of conciseness, we ignore the role of fluctuations (but see *e.g* David *et al.* [180]).

This section is organised as follows. We present a generic effective free energy

constructed on the basis of symmetry considerations and conservation laws. From this energy, we find interesting phenomena, namely local shifts in the binodal concentrations and a curvature dependence of the line tension. To shed light on the origin of the phenomenological parameters in the free energy, we construct a curved space generalisation of the two-dimensional lattice gas model. We concentrate on dumbbell-shaped surfaces. To gain fundamental insights into the antimixed state, first, we approximate the shape of the dumbbell as two disjointed spheres able to exchange lipids. Then, we prove that the antimixed state also persists on a dumbbell-shaped membrane with a neck.

4.3.1 Scalar field theory on curved backgrounds. We now consider a two-dimensional binary fluid and assume that all the relevant degrees of freedom can be captured by a single, generally space-dependent, and scalar order parameter $\phi = \phi(\boldsymbol{r})$. Using a single field has numerous advantages, as it roots in the classical theory of phase separations and was first used to model the interaction between curvature and lipid lateral organisation by Markin[156] and Leibler[57].

If the fluid is incompressible and the average area per molecule is the same for both components, ϕ can be interpreted as the absolute concentration of either one of the two components:

$$\phi = \frac{[A]}{[A] + [B]} \,, \tag{4.25}$$

where $[\ldots]$ indicates the concentration of the A and B molecules. By construction, $0 \leq \phi \leq 1$ and any value other than $\phi = 0$ or $\phi = 1$ indicates local mixing of the two components. The system is defined on an arbitrarily curved surface S. We assume that S is fixed so that the local geometry can influence the configuration of the order parameter ϕ, but not *vice versa*. The most general free energy functional of such a system will then be of the form:

$$F = \int_S dA\, \mathcal{F}(\phi, \nabla\phi, S) \,, \tag{4.26}$$

where $\mathcal{F}$ is a generic free energy density depending on ϕ, its surface-covariant gradient $\nabla\phi$, and the surface shape S. Here,

$$dA = dxdy\sqrt{\det h}$$

where $\{x, y\}$ are the local coordinates, $dxdy$ is the surface area element, and $\det h$ is the determinant of the first fundamental form on S.

In practice, the explicit form of $\mathcal{F}$ can be obtained upon coarse-graining a microscopic model over a mesoscopic portion of S. Such portion should be small compared to the size of the whole system and yet large compared to typical molecular length-scales, which we call a. Alternatively, as in most cases of practical interest, $\mathcal{F}$ is constructed phenomenologically, on the basis of symmetry arguments and physical insight. Because the order parameter is generally non-uniform across the surface, the gradient $\nabla\phi$ introduces new length scales in the system. Here we assume that the spatial variation of the order parameter occurs on a length scale much larger than the molecular size, namely: $|\nabla\phi| \sim \epsilon^{-1} \ll a^{-1}$. Moreover, at physical equilibrium, gradients are always negligible

with the only possible exception for isolated quasi-one-dimensional regions where the spatial variation of the order parameter can be more pronounced. As we will explain later, these regions correspond to diffuse interfaces between bulk phases and, being lower dimensional structures, do not affect the bulk value of the free energy. Since integrated variations have to be finite, ϵ also sets the typical thickness of these interfaces.

The symmetries of Equation 4.26 dictate how $\mathcal{F}$ can depend on the shape of S. If the fluid is isotropic (*i.e.* molecules do not have a specific direction on the tangent plane of S), $\mathcal{F}$ depends on the surface either intrinsically, through the Gaussian curvature K, or extrinsically, through the mean curvature H. Furthermore, if the molecules are insensitive to the orientation of the surface (*i.e.* they do not discriminate convex from concave shapes), $\mathcal{F}$ must be invariant for $H \to -H$, since, on orientable surfaces, the sign of H depends uniquely on the choice of the normal direction. Thus $\mathcal{F}$ depends on the curvature only through H^2, K and, in principle, their derivatives. Non-vanishing curvatures introduce further length scales in the system, which we collectively denote as R and assume larger or equal to ϵ, thus $R \geq \epsilon \gg a$.

Now, expanding Equation 4.26 to the second order in the gradients and the curvatures (thus with respect to a/ϵ and a/R) yields:

$$\mathcal{F} \simeq \frac{D(\phi)}{2} |\nabla\phi|^2 + f(\phi) + k(\phi)H^2 + \bar{k}(\phi)K + \cdots , \tag{4.27}$$

where D, f, k and $\bar{k}$ are the resulting coefficients in the Taylor expansion and the dots indicate higher order terms. These coefficients depend, in general, on the local order parameter ϕ and cannot be determined from symmetry arguments. To render Equation 4.27 dimensionless, we rescale all the terms by a constant energy density, in such a way that f is dimensionless, whereas D, k and $\bar{k}$ have dimensions of area.

The physical meaning of the various terms in Equation 4.27 is intuitive and has been thoroughly discussed in literature of phase field models[174;175] and lipid membranes[181]. To have an energy bounded from below requires $D \geq 0$, so that the first term promotes uniform configurations of the order parameter. This term originates from the short-range attractive interactions between molecules and gives rise to a concentration-dependent diffusion coefficient[168;176;182;183]. Notice that D does not depend on the curvatures, because of the quadratic truncation underling Equation 4.27. Higher order terms coupling the order parameter gradients and the curvature tensor have been discussed elsewhere[184–187] and will not be considered here. The function f is the local thermodynamic free energy in flat space. This includes both energetic and entropic contributions, promoting phase separation and mixing, respectively. In the case of fluctuating surfaces, such as lipid membranes, f could be interpreted as a concentration-dependent surface tension. Finally, k and $\bar{k}$ are, respectively, the bending and saddle splay moduli of the mixture, expressing the energetic cost, or gain, of having a given configuration of the field ϕ, in a curved region of the surface. Analogously to f, for a fluctuating surface these terms could be interpreted as a curvature-dependent contributions to the surface tension, introducing a departure for the flat-space value. The length scale associated to these deviations is commonly known as Tolman length[188]. A generic surface may have up to two independent Tolman lengths.

For systems sensitive to the orientation of the surface, such as Langmuir monolayers and asymmetric lipid bilayers, the expansion Equation 4.27 is not required to be invariant for $H \to -H$ and can feature linear contributions of the form cH, with $c = c(\phi)$ a coupling coefficient, equivalent to a concentration-dependent spontaneous curvature $H_0 = -c/(2k)$. For simplicity, we will ignore this contribution, even if most of our results can be easily extended to this case.

Equilibrium configurations are defined as the minima of the free energy functional Equation 4.26. Here we focus on closed systems, where the order parameter is globally conserved. Thus:

$$\Phi = \frac{1}{A_S}\int_S \mathrm{d}A\,\phi = \text{const}\,, \tag{4.28}$$

with A_S the area of the surface. The problem then reduces to finding the function ϕ minimising the constrained free energy:

$$G = F - \hat{\mu}\Phi\ , \tag{4.29}$$

where $\hat{\mu}$ is the Lagrange multiplier enforcing the constraint described in Equation 4.28. For homogeneous systems, $\hat{\mu}$ is the chemical potential, thermodynamic conjugate of the concentration. The first functional derivative of G yields the equilibrium condition

$$f'(\phi) \;+\; k'(\phi)H^2 \;+\; \bar{k}'(\phi)K \quad = \quad D(\phi)\nabla^2\phi \;+\; \frac{1}{2}D'(\phi)|\nabla\phi|^2 \;+\; \mu\,, \tag{4.30}$$

where the prime indicates differentiation with respect to ϕ (*i.e.* $f' = \partial f/\partial\phi$), $\nabla^2 = h^{ij}\nabla_i\nabla_j$ is the Laplace-Beltrami operator on S, and $\mu = \hat{\mu}/A_S$ is the chemical potential density. Equation 4.30 is too generic to draw specific conclusions, unless the $\phi-$dependence of the various coefficients is specified. Later we will consider a specific lattice model, but, before then, it is useful to review the case of homogeneous potentials and make some general consideration on the linearisation of inhomogeneous terms.

Homogeneous potential on a flat surface

We first consider a binary mixture in a homogeneous potential. To do this, we use a flat and compact surface for S consisting of a rectangular domain with periodic boundaries. Since both the mean and Gaussian curvature are equal to zero and assuming that field variations are small, Equation 4.30 reduces to:

$$f'(\phi) = \mu\,. \tag{4.31}$$

If f is convex, the single homogeneous phase $\phi = \Phi$ is a solution of Equation 4.31, corresponding to a stable thermodynamic state, where the two components of the mixture are homogeneously mixed with one another. We refer to this configuration as the mixed phase. Consistently we must have:

$$\mu = f'(\Phi)\ , \qquad \frac{G}{A_S} = f(\Phi) - f'(\Phi)\Phi\ .$$

If, on the other hand, f is concave for some ϕ values (*i.e.* $f'' < 0$), then the mixed phase might become unstable and it is energetically favourable to split the system into, at least, two regions where ϕ takes different values, ϕ_- and ϕ_+. We refer to this configuration as the demixed, or phase-separated phase:

$$\phi(\boldsymbol{r}) = \begin{cases} \phi_+, & \boldsymbol{r} \in S_+ \\ \phi_-, & \boldsymbol{r} \in S_- \end{cases} , \tag{4.32}$$

where $S_\pm$ are the two domains into which S partitions (Figure 4.6).

Now, let $A_\pm = \int_{S_\pm} dA$ to be the respective areas and $\varphi_\pm = A_\pm / A_S$ to be their relative area fraction, with $\varphi_+ + \varphi_- = 1$. As a result, the total fixed concentration is:

$$\Phi = \varphi_+ \phi_+ + \varphi_- \phi_- \, . \tag{4.33}$$

Since ϕ is assumed to vary smoothly over a region of negligible area, it is possible to formally integrate Equation 4.31 with respect to ϕ and obtain the set of equilibrium conditions:

$$\mu = f'(\phi_\pm) = \frac{f(\phi_+) - f(\phi_-)}{\phi_+ - \phi_-} \, , \tag{4.34}$$

known as the Maxwell common-tangent construction, see Figure 4.7. The interval of Φ values for which we have the demixed phase, Equation 4.32, is the true minimum of the free energy. Thus, a mixed phase with a total concentration Φ in the interval $\phi_- < \Phi < \phi_+$, but such that $f''(\Phi) > 0$, is metastable, since such a phase can still resist small perturbations. The field values $\phi_\pm$ are known as binodal points, the interval $[\phi_-, \phi_+]$ is known as the miscibility gap, whereas the concentrations for which $f''(\phi) = 0$ are known as spinodal points.

If we consider spatial variations of the order parameter ϕ, Equation 4.30 reduces to:

$$f'(\phi) = \mu + \epsilon^2 \nabla^2 \phi \, , \tag{4.35}$$

with $\epsilon^2 = D$. Since f' is, in general, a nonlinear function of ϕ, Equation 4.35 is often analytically intractable. However, as long as ϵ is much smaller than the system size, Equation 4.32, is still a valid solution over large portions of S.

Homogeneous potential on curved surfaces

We now consider the more generic case in which S has non-vanishing curvatures H and K, but no explicit coupling with the order parameter, by setting $k = \bar{k} = 0$ in Equation 4.27. This scenario occurs, for instance, in mixtures whose components are equally compliant to bending, thus there is no energetic preference for the order parameter ϕ to adjust to the underlying curvature of the surface. Yet, as any interface in the configuration of the field ϕ costs a finite amount of energy, roughly proportional to the interface length, the shape of S indirectly affects the spatial organisation of the binary mixture *via* the geometry of interfaces.

Upon demixing, the system drives the formation of interfaces. This means that in regions of thickness $\approx \epsilon$ the field ϕ is smoothly interpolating between the bulk values of

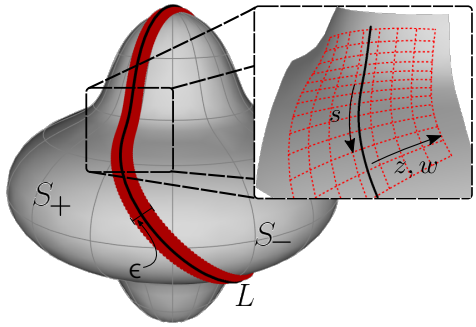

Figure 4.6: Phase separation on a surface S. When the system phase-separates, the surface S is divided into two regions $S_\pm$. The thin interface L separating them is a curved strip of finite geodesic width $\sim \epsilon$, shown in red. In reality we require ϵ to be much smaller than any macroscopic length scale. In order to study the behaviour of $\phi(x)$ near the interface, we need to construct an adapted geodesic frame, spanned by the coordinates s, the arc-length parameter of the sharp interface (shown in black), and by the normal arc-length coordinate $z = w/\epsilon$. Constant s lines are geodesics of S.

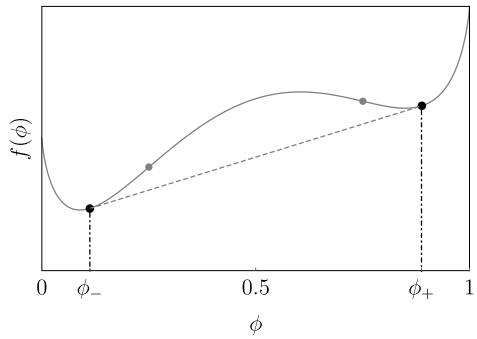

Figure 4.7: Free energy of a demixed state. For concave free energies the thermodynamic minimum is attained by demixed configurations when the total concentration Φ lies within the miscibility gap. We show respectively in black and gray the binodal and spinodal points relative to $f(\phi)$. The diagonal dashed line is the common tangent which defines, *via* Equation 4.34, the binodal points. For a given Φ, the area fractions $\varphi_\pm$ of the A and B components are found with the lever rule, *i.e.* by solving Equation 4.33 combined with $\varphi_+ + \varphi_- = 1$.

the two phases. Since we are in a regime where this thickness is much smaller than the size of the system, we can take Equation 4.35 and expand it in powers of ϵ. In the proximity of L, we need to adapt the coordinate system to take into account both the curvature of the interface, as a strip embedded on the surface, and of the intrinsic curvature of the surface itself. Then, we can treat the scalar field as a function of coordinates in this frame, $\phi = \phi(s, z)$, where s is the arc-length parameter of the sharp interface L and z is the normal geodesic distance from the curve. Furthermore, variations along z happen on a scale $\sim \epsilon$, while variations along s become relevant only at macroscopic distances. This implies that ϕ is a function of only the normal coordinate z up to at least order ϵ^2, and we can rescale the variable $z \to w/\epsilon$ so that the values $w \to \pm\infty$ correspond to the bulk phases.

With this construction at hand, we collect the various terms in 4.35, order by order in ϵ, and solve iteratively the differential equation. At $O(1)$ we find the so-called profile equation, which, after matching with the bulk values of ϕ away from the interface, reads:

$$\frac{1}{2}x(w)^2 = g(x)\,, \tag{4.36}$$

where $x(w) = \phi(z/\epsilon)$ is the order parameter expressed as function of the rescaled normal coordinate w, and g is the shifted potential

$$g(x) = f(x) + \frac{(\phi_- - x)f(\phi_+) - (\phi_+ - x)f(\phi_-)}{\phi_+ - \phi_-}\,, \tag{4.37}$$

which has the properties $g(\phi_\pm) = g'(\phi_\pm) = 0$ and $g''(x) = f''(x)$, *i.e.* g shares the same binodal points with f. Typically, solutions of Equation 4.36 decay exponentially towards the bulk phases and interpolate monotonically between the two phases. As we shall later see, this will not necessarily be the case for non-homogeneous systems.

Solving Equation 4.35 at $O(\epsilon)$ is slightly more involved, but leads to a series of simple and interesting results. First, in regions where $\epsilon^2 K$ is small, the equilibrium interface must obey the interface equation (Equation 4.1):

$$\kappa_g = \text{const}\,, \tag{4.38}$$

with κ_g the geodesic curvature of the interface L. From this equation it can be shown that a non geodesic interface induces a modification of the equilibrium chemical potential, which leads:

$$\mu = \frac{f(\phi_+) - f(\phi_-)}{\phi_+ - \phi_-} + \frac{\sigma\kappa_g}{\phi_+ - \phi_-}\,, \tag{4.39}$$

where we introduced the interfacial line tension σ, defined as:

$$\sigma = \epsilon \int_{\phi_-}^{\phi_+} dx \sqrt{2g(x)}\,. \tag{4.40}$$

Equation 4.39 implies that, for non-geodesic interfaces, equilibrium bulk concentrations slightly deviate from the Maxwell values. This phenomenon is entirely absent in phase separations of open systems, where instead the bulk phases concentrations are not affected by the interface curvature.

Inhomogeneous potential on curved surfaces

We finally consider the most generic scenario in which all terms in Equations 4.27 and 4.30, including k and $\bar{k}$, are non-vanishing. In this case the local curvature affects directly the magnitude of the order parameter ϕ, instead of indirectly influencing lateral displacement of the domains. Without specifying the shape of S or the functional form of $k(\phi)$ and $\bar{k}(\phi)$, it is hard to make precise predictions. We will deal with a specific model and specific geometries in the next section.

Here, we consider instead an approximately flat membrane, so we can treat the curvature terms as perturbations. If $k(\phi)H^2$ and $\bar{k}(\phi)K$ are much smaller than f, we obtain that the binodal points of the free energy are shifted by a small, curvature-dependent, amount. More precisely, we find that the Maxwell values are shifted as $\phi_\pm \to \phi_\pm + \delta\phi_\pm$, with:

$$\delta\phi_\pm = \frac{\Delta k H^2 + \Delta\bar{k}K}{\phi_+ - \phi_-} - \frac{k(\phi_\pm)H^2 + \bar{k}(\phi_\pm)K}{f''(\phi_\pm)} \,, \tag{4.41}$$

where $\Delta k = k(\phi_+) - k(\phi_-)$ and $\Delta\bar{k} = \bar{k}(\phi_+) - \bar{k}(\phi_-)$ are the differences between the bending moduli evaluated on the homogeneous binodal concentrations. Equation 4.41 shows that the equilibrium bulk phases are directly influenced by local curvature.

4.3.2 A curvature modified lattice-gas model. To draw precise conclusions for binary mixtures with inhomogeneous potential on curved surfaces, it is indispensable to make the $\phi-$dependence of the functions D, f, k, and $\bar{k}$ in Equation 4.27 explicit. Thus we focus our analysis on a specific subset of possible material properties. Although this operation can be performed in multiple ways, here we propose a simple and yet insightful strategy based on a curved-space generalisation of the most classic microscopic model of phase separation, namely the lattice-gas model. To this purpose, we discretise S into a regular lattice, with coordination number q and lattice spacing a. Each site is characterised by a binary spin $s_i = \pm 1$, serving as a label for either one of the molecular components.

Because of the short range interactions between the molecules, the total energy of the system is computed *via* the Ising Hamiltonian:

$$\mathcal{H} = -\sum_{\langle ij \rangle} J_{ij} s_i s_j - \sum_i h_i s_i \,, \tag{4.42}$$

where $i = 1, 2 \dots N$ and $\langle ij \rangle$ indicates a sum over all the pairs of nearest neighbours in the lattice. Finally, conservation of the total number of molecules implies:

$$\sum_i \left(\frac{1 + s_i}{2} \right) = \Phi N \,. \tag{4.43}$$

In the classic lattice-gas model, the coupling constant J_{ij} and the external field h_i are uniform across the system. Here, we allow them to depend on the local geometry of S. Using the same assumptions underlying the expansion of Equation 4.27, augmented by

the additional symmetry $J_{ij} = J_{ji}$, yields:

$$J_{ij} = \frac{1}{4}\left(J + Q_k\,\frac{H_i^2 + H_j^2}{2} + Q_{\bar{k}}\,\frac{K_i + K_j}{2}\right)\,, \tag{4.44a}$$

$$h_i = -\frac{1}{2}\left(L_k H_i^2 + L_{\bar{k}} K_i\right)\,, \tag{4.44b}$$

where H_i and K_i are, respectively, the mean and Gaussian curvature evaluated at the $i-$th lattice site. The $Q-$couplings modulate the relative strength of the attraction/repulsion between molecules, reflecting that both the distance and relative orientation of neighbouring molecules vary across the surface. Similarly, the $L-$couplings measure the propensity of a molecule to adapt to the local curvature. In particular, we note that $L_{\bar{k}}$ is exactly the only curvature coupling employed by Paillusson *et al.*[170] to describe the interaction of binary mixtures with minimal surfaces. We stress that, in order for the Hamiltonian in Equation 4.42 to admit phase separation, $J_{ij} > 0$. As the local Gaussian curvature can be both positive and negative, this is not necessarily true for a generic surface and an arbitrary choice of the constants J, Q_k and $Q_{\bar{k}}$. In the following, we assume that $J > 0$ is sufficiently large to prevent J_{ij} from changing sign. Furthermore, we assume for simplicity that all the other constants in Equations 4.44 are positive. The latter assumption is not indispensable and has no qualitative effects on the structure of the free-energy landscape or on the phase diagram.

The free energy of the mixture can easily be calculated now using the mean-field approximation, upon assuming the variables s_i to be spatially uncorrelated (*i.e.* $\langle s_i s_j\rangle = \langle s_i\rangle\langle s_j\rangle$, with $\langle\cdots\rangle$ the ensemble average). Thus, letting:

$$P(s_i) = \phi_i \delta_{s_i,1} + (1-\phi_i)\delta_{s_i,-1}\,, \tag{4.45}$$

the probability associated with finding a molecule of type A or type B at $i-$th site, yields, after standard algebraic manipulations[189],

$$F = -\sum_{\langle ij\rangle} J_{ij}(2\phi_i - 1)(2\phi_j - 1) + \sum_i h_i(2\phi_i - 1) + T\sum_i \left[\phi_i \log\phi_i + (1-\phi_i)\log(1-\phi_i)\right]\,, \tag{4.46}$$

with T the temperature in units of k_B. Coarse-graining Equation 4.46 over the length scale ϵ, finally yields Equations 4.26 and 4.27, with:

$$D(\phi) = \epsilon^2 J\,, \tag{4.47a}$$

$$f(\phi) = qJ\phi(1-\phi) - T\mathcal{S}(\phi)\,, \tag{4.47b}$$

$$k(\phi) = qQ_k\phi(1-\phi) + L_k\phi\,, \tag{4.47c}$$

$$\bar{k}(\phi) = qQ_{\bar{k}}\phi(1-\phi) + L_{\bar{k}}\phi\,, \tag{4.47d}$$

where $\mathcal{S}(\phi) = -\phi\ln\phi - (1-\phi)\ln(1-\phi)$ is the mixing entropy.

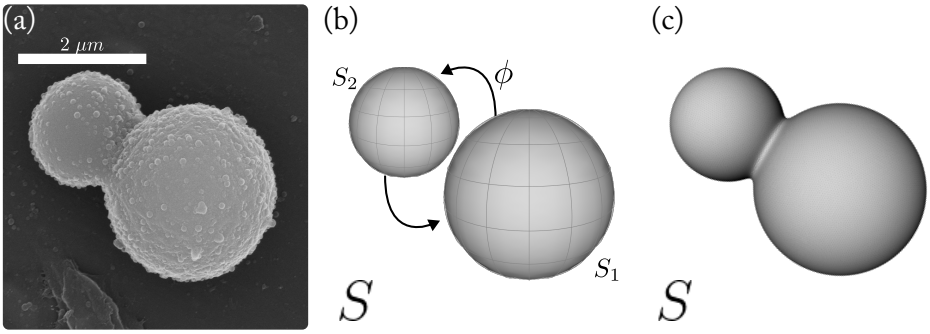

Figure 4.8: The disjointed spheres model. (a) Experimental scanning electron microscopy image of an asymmetric dumbbell-shaped colloid used as scaffold for the lipid membrane. **(b)** Approximation of the surface in (a) as two disconnected spheres exchanging order parameter ϕ. **(c)** Full three-dimensional reconstruction of the dumbbell.

The phase diagram of disjointed spheres

We now focus on asymmetric dumbbell-shaped substrates, such as the one depicted in Figure 4.8. We approximate S with a closed system consisting of two disjoint spheres, S_1 and S_2, of different radii, allowed to exchange molecules with one another, as shown in Figure 4.8b. This results into the following constraint for the total concentration Φ:

$$\sum_{a=1,2} \varphi_a \Phi_a = \Phi \,, \tag{4.48}$$

where $\Phi_a = 1/A_a \int_{S_a} dA\, \phi$, is the average concentration over the S_a sphere ($a = 1, 2$), with $A_a = 4\pi R_a^2$ the sphere area and R_a the radius. Analogously, $\varphi_a = A_a/A_S$ represents the area fraction of each sphere. Equation 4.30 can now be solved using the mean field parameter given by Equations 4.47, averaged over each sphere. Since for spheres $H^2 = K = R^{-2}$, the four geometric couplings of Equations 4.47 become pairwise equivalent, thus reducing the number of independent parameters to two: a symmetry-preserving quadratic term and a symmetry-breaking linear term.
To see this explicitly we first minimise the free energy separately on each sphere, which gives the equations

$$1 - 2\Phi_a = \tanh \frac{T_L^{(a)} + 2T_c^{(a)}\,(1 - 2\Phi_a) - \mu}{2T} \,, \tag{4.49}$$

where we defined the local critical temperature,

$$T_c^{(a)} = \frac{q}{2}\left(J + \frac{Q_k + Q_{\bar{k}}}{R_a^2}\right) \,, \tag{4.50}$$

and we introduced the curvature-dependent energy scale associated with the linear coupling,

$$T_L^{(a)} = \frac{L_k + L_{\bar{k}}}{R_a^2} \,. \tag{4.51}$$

Constructing the equilibrium phase diagram of this system is a two-step process. First, one must find the values Φ_a satisfying Equation 4.49 and the constraint of Equation 4.48. Once these have been found, one must check the stability of each average concentration against spontaneous phase separation, *i.e.* verify whether Φ_a lies within the local miscibility gap $[\phi_-^{(a)}, \phi_+^{(a)}]$ on each sphere.

For fixed values of temperature and curvature couplings, the solutions of Equation 4.49 define a family of curves in the $\{\Phi_1, \Phi_2\}$ plane, as the total concentration Φ is smoothly changed from 0 to 1. We refer to these curves as "lines of equilibrium" and show some examples of them in Figure 4.9. Although smooth, these lines do not need to be connected. Mathematically, they correspond to the set of points in concentration space where the gradient of the free energy is proportional to the vector $\{1, 1\}$. Figure 4.9a shows the effect of varying the local critical temperature $T_c^{(a)}$ on each sphere. Since the free energy is still symmetric under the exchange $\phi \leftrightarrow 1 - \phi$, the lines of equilibrium are invariant under the mapping $\Phi_a \to 1 - \Phi_a$. Different colours correspond to different $Q_k + Q_{\bar{k}}$ values in Equation 4.50, ranging from 0 (red) to $1/10\ qJR_1^2$ (blue). All curves pass through $\Phi_1 = \Phi_2 = 1/2$. Figure 4.9b shows the effect of the linear $L-$couplings: $L_k + L_{\bar{k}}$ is increased from 0 (red) to $1/20\ qJR_1^2$ (blue). In both panels the temperature is $T = 9/2\ qJ$, and the spheres have radii $R_1 = 1$ and $R_2 = 2/3$.

It is instructive to compare, in closer detail, these results with those obtained in the absence of explicit coupling between the order parameter and the curvature, namely: $T_L^{(a)} = 0$ and $T_c^{(1)} = T_c^{(2)}$ (the red-most lines in both panels). In this case, the lines of equilibrium consist of two mutually intersecting curves: a diagonal straight line $\Phi_1 = \Phi_2 = \Phi$, corresponding to the usual homogeneously mixed phase, and a second oval-shaped closed curve. The latter curve implies the existence of a second branch of solutions, where the amount of order parameter on each sphere is different from the total average. This result might be surprising, given that in this case the free energy density is homogeneous. However, it can be easily argued that this is an artefact of our model, originating from the following two arguments. First, the geometry we are considering is exceptional: the two spheres are not in direct contact and having $\Phi_1 \neq \Phi_2$ does not cost any extra interfacial energy, as it would be the case for a single connected surface. In fact, non-zero gradients would be strongly disfavoured. Secondly, it can be verified that the oval always lies within the miscibility gap of the potential and, therefore, even if mathematically possible, these extra solutions are thermodynamically metastable at best. This case alone shows another, rather general, fact: for a given set of external parameters, there can be multiple pairs of solutions of Equation 4.49, each corresponding to a possible (meta)stable equilibrium state.

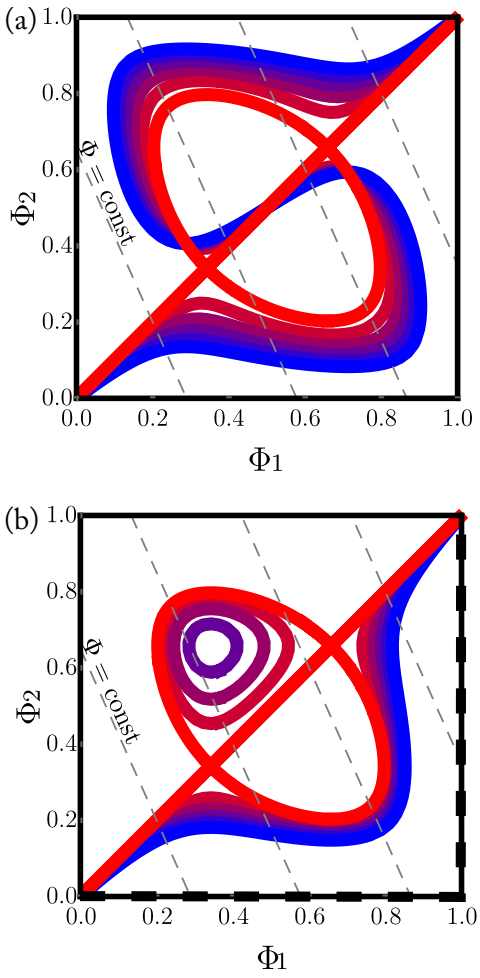

Figure 4.9: Lines of equilibrium. Solutions of Equation 4.49 for two spheres with radii ratio $R_2/R_1 = 2/3$ at sub-critical temperature $T = 0.45\,qJ$. **(a)** Lines have all $T_L^{(a)} = 0$ but regularly increasing $T_c^{(a)}$ from $1/2\,qJ$ (red) to $(1/2 + 1/10R_a^{-2})\,qJ$ (blue). **(b)** Lines have all $\Delta T_c = 0$ while $T_L^{(a)}$ increases from 0 (red) to $1/20\,R_a^{-2}qJ$ (blue). The black, thick, dashed line corresponds to the infinite $T_L^{(a)}$ limit. Diagonal dashed lines are of constant Φ.

Spatial curvature changes this picture by introducing a smooth deformation of the lines of equilibrium. In Figure 4.9a the straight line and the oval merge together into a single S-shaped connected curve, while in Figure 4.9b one portion of the oval and of the straight line merge into a single line, and the rest splits into a closed curve. The latter becomes smaller and smaller as $T_L^{(a)}$ increases, and eventually disappears, leaving a single branch of equilibrium solutions. Our sign choices are such that it is thermodynamically preferable to first build-up non-zero ϕ on the largest sphere up to its maximum capacity (*i.e.* $\Phi_1 \approx \Phi$ and $\Phi_2 \approx 0$), rather than keeping the concentration everywhere uniform. Hence, at small Φ, the lines of equilibrium bend towards the lower-right half of the diagram. For the linear coupling, this trend continues until the larger sphere is almost saturated. Then the concentration starts increasing on the small sphere too (so that the closed curves in the top left of Figure 4.9b are always metastable). For the quadratic coupling the situation is more symmetric, in such a way that, for larger Φ values, it is more convenient to have a higher concentration on the small sphere. Note that, because of the classic double-well structure of the thermodynamics potentials, for a given Φ value there can be up to three different equilibrium solutions. Regardless of these quantitative differences, the main qualitative feature of the toy-model described in this Section is that, as a consequence of the influence of curvature on the free energy landscape of the binary mixture, the two disjoint spheres exhibit different concentrations despite being still in the "mixed" phase, *i.e.* without developing any interface. Interestingly, this phenomenon has some similarity with the thermodynamics

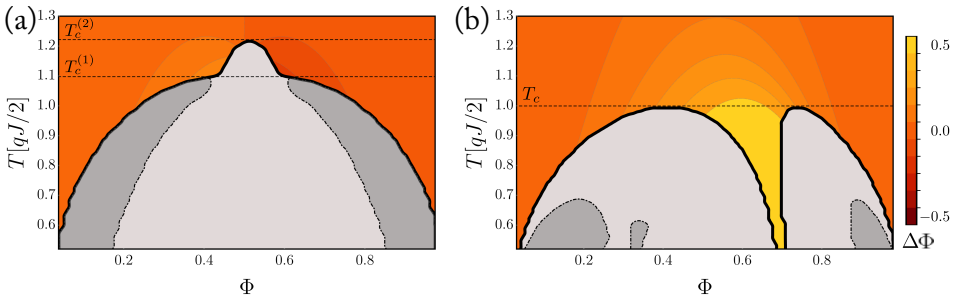

Figure 4.10: Equilibrium phase diagrams in the presence of curvature interactions for the two-spheres system of Figure 4.8b with $R_1 = 1$ and $R_2 = 2/3$. The solid black lines separate the mixed (different shades of red/yellow corresponding to degrees of inhomogeneity as shown in the legend) from the partially demixed phase (lighter gray). All transition lines are binodals. **(a)** Effect of the quadratic coupling, with $Q_k + Q_{\bar{k}} = 1/5\, R_1^2 qJ$. Each sphere has a different critical temperature, namely $T_c^{(1)} = 0.55\, qJ$ and $T_c^{(2)} = 0.65\, qJ$. Since $\Delta T_L = 0$, the diagram is symmetric for $\Phi \to 1 - \Phi$. The inhomogeneity of the mixed phase is small and relevant only in the proximity of the critical temperatures. **(b)** Effect of the linear coupling, with $L_k + L_{\bar{k}} = 1/10\, R_1^2 qJ$. The critical temperature is the same for both spheres at $T_c = 1/2\, qJ$. The generalised mixed phase is strongly inhomogeneous in the region below T_c and for concentrations $\Phi \sim \varphi_1 \sim 0.69$.

of lipid membranes adhering onto non-homogeneous flat substrates[126].

Figure 4.10 shows the phase diagram of the system, obtained upon varying the temperature T and the total concentration Φ, while keeping $T_c^{(a)}$ and $T_L^{(a)}$ fixed. To highlight the specific role of each of these couplings, we isolate the effect of the quadratic coupling in Figure 4.10a and that of the linear couplings in Figure 4.10b, by setting $T_L^{(1)} = T_L^{(2)}$ and $T_c^{(1)} = T_c^{(2)}$, respectively. We observe three stable phases: a mixed phase with no interfaces (red/yellow shades), a partially demixed phase with interfaces only on one sphere (lighter grey), and finally a fully demixed phase with phase separation occurring on both spheres (darker grey). To better characterise the mixed phase we introduce the difference:

$$\Delta\Phi = \Phi_1 - \Phi_2\,, \tag{4.52}$$

which quantifies the departure of the concentration on a single sphere from the total average and it is indicated by different shades of red/yellow in Figure 4.10. A completely homogeneous mixed phase would then have $\Delta\Phi = 0$. The different shades of red/yellow in Figure 4.10 indicate different values of $\Delta\Phi$, as shown in the legend. From the diagrams it is clear that, even in absence of genuine phase separation, one needs to relax and generalise the notion of mixing in order to grasp the complexity of the current scenario in comparison to the traditional picture. In fact, outside local miscibility gaps the "mixed" phase has a non-zero $\Delta\Phi$. This effect is enhanced when there is a linear coupling, as in Figure 4.10b, especially below T_c and for concentrations close to the relative area ratio of the two spheres, $\Phi \sim \varphi_1$ (which is equal to ~ 0.69 in the Figure).

Before dwelling into a detailed description of this phenomenon, let us emphasise that what we call here inhomogeneous mixing, is not a new thermodynamic phase, but rather the generalisation of mixing to macroscopically non-homogeneous closed systems. In fact, the effect of inhomogeneities is smoothly smeared out at high temperatures, where the usual homogeneous mixing is always the true equilibrium.

To see this, consider the limit where $T \gg T_c^{(a)}$ and $T \gg T_L^{(a)}$. We can then linearise the curvature couplings in Equation 4.49 and solve the equilibrium equation perturbatively. To this purpose, let us introduce the average critical temperature

$$\hat{T}_c = \frac{T_c^{(1)} + T_c^{(2)}}{2}\,, \tag{4.53}$$

and the two energy scale differences

$$\Delta T_c = \frac{T_c^{(1)} - T_c^{(2)}}{2}\,, \quad \Delta T_L = \frac{T_L^{(1)} - T_L^{(2)}}{2}\,. \tag{4.54}$$

By expanding Equation 4.49 at first order in ΔT_c and ΔT_L, we get the deviation of the local concentrations from the total average

$$\Delta\Phi = C_Q(\Phi, \hat{T}_c/T)\frac{\Delta T_c}{T} - C_L(\Phi, \hat{T}_c/T)\frac{\Delta T_L}{T}\,. \tag{4.55}$$

The only relevant property of C_Q and C_L is that they take finite values in the large T limit, namely

$$C_Q(\Phi, 0) = 4\Phi(1-\Phi)(2\Phi - 1)\,, \tag{4.56a}$$
$$C_L(\Phi, 0) = 2\Phi(1-\Phi)\,. \tag{4.56b}$$

Equation 4.55 clearly shows that, regardless of the magnitude of the curvature couplings, homogeneous mixing is always restored at high temperature. Furthermore, as the free energy is a continuous function of the concentrations Φ_a, such a crossover between inhomogeneous and homogeneous mixing occurs continuously, *i.e.* without passing through a first order phase transition. This argument can straightforwardly be extended to any arbitrary perturbative order in ΔT_c and ΔT_L, demonstrating that equilibria with $\Delta\Phi \neq 0$ and $\Delta\Phi = 0$ corresponds to different states of the same phase.

Although spatial curvature does not give rise to additional thermodynamic phases, its effect below the critical temperature is nonetheless dramatic, as indicated by Figure 4.10b. In this region of the phase diagram, the miscibility gaps splits in two disconnected sections, separated by an intermediate continuum of states where $\Delta\Phi$ is large, hence the concentration on the two spheres is highly non-homogeneous. We have reported in this thesis in Chapter 3 a direct experimental observation of these states and termed them antimixed states.

An intuitive understanding of this phenomenon can be achieved by considering the limiting case in which $|\Delta T_L|$ surpass any other energy scale. In this limit, the phase

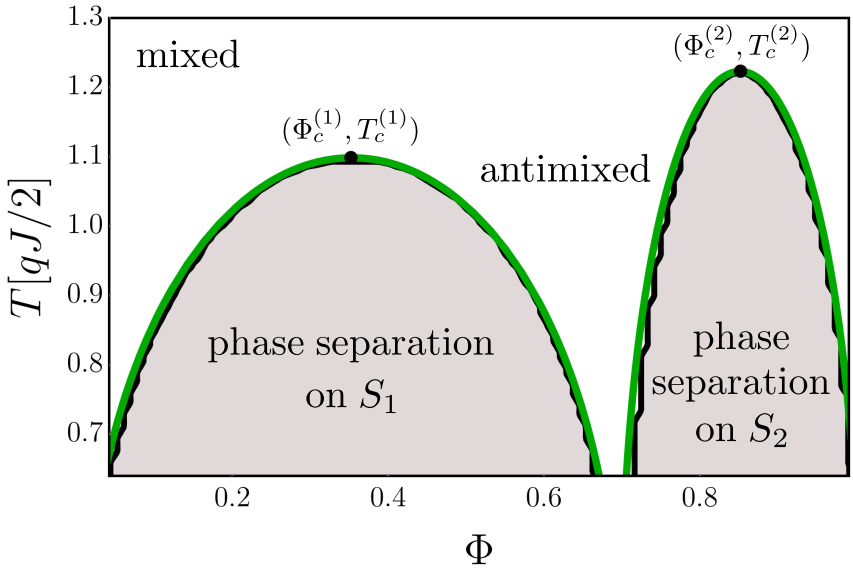

Figure 4.11: The equilibrium phase diagram in the strong linear coupling limit. This figure is analogous to Figure 4.10, with non-zero linear and quadratic couplings: we set $Q_k + Q_{\bar{k}} = 1/5\, R_1^2 qJ$ and $L_k + L_{\bar{k}} = 7/4\, R_1^2 qJ$. The critical temperatures on each sphere are $T_c^{(1)} = 0.55\, qJ$ and $T_c^{(2)} = 0.65\, qJ$. The green lines are the analytic binodal lines obtained from Equation 4.57. In the lighter grey region where phase separation happens on S_1, we have $\Phi_2 = 0$. Conversely, in the region where phase separation happens on S_2, we have $\Phi_1 = 1$. The two black dots are the critical points relative to each sphere, with critical concentrations given by Equation 4.58.

diagram becomes a disjoint union of the phase diagrams of each subsystem, given the simple mapping between Φ_a and Φ. This is illustrated in Figure 4.11. Analysing the stability of the mixed phase on each sphere leads to the conclusion that global phase separation is impossible in such a large $|\Delta T_L|$ limit, since there is no overlap between miscibility gaps of the two spheres. Moreover, the binodals of each sphere (the green lines in Figure 4.11) can be analytically derived:

$$T_{\text{binodal}}^{(1)} = \mathcal{T}\left(\frac{\Phi}{\varphi_1}\right), \tag{4.57a}$$

$$T_{\text{binodal}}^{(2)} = \mathcal{T}\left(\frac{\Phi - \varphi_1}{\varphi_2}\right), \tag{4.57b}$$

with $\mathcal{T}(y) = (1-2y)/\text{arctanh}(1-2y)$. There are two distinct critical points of the system, specific to a single sphere, located at $\{\Phi_c^{(a)}, T_c^{(a)}\}$ in the phase diagram (as shown in Figure 4.11). The two critical temperatures are given by Equation 4.50, while the critical

concentrations are:

$$\Phi_c^{(1)} = \frac{\varphi_1}{2} \quad , \quad \Phi_c^{(2)} = \varphi_1 + \frac{\varphi_2}{2} \, , \tag{4.58}$$

where $\{\varphi_1, \varphi_2\}$ are the relative area fractions in the two spheres. With this analytical results in hand, it is then possible to give a precise definition of the antimixed state: we define antimixed as the mixed phase of an inhomogeneous binary fluid at sub-critical temperature with non-overlapping local miscibility gaps.

Now, from a strictly technical point of view, it may be argued that our treatment of the substrate geometry is oversimplified, as we approximate the dumbbell-shaped membrane of Figure 4.8a with the two disjoint spheres of Figure 4.8b. Evidently, a real membrane is a single structure, and having $\Delta\Phi \neq 0$ will inevitably induce gradients in the neck region that interpolates between the two lobes. Could these interfacial effects destroy the antimixed state? This question is addressed in the following section.

4.3.3 The phase diagram of spheres connected with a neck. In this section, we test whether our predictions of the existence of inhomogeneous mixing and antimixed hold for more realistic geometries, which are able to support interfaces of finite length. In particular, we verify whether these bulk equilibrium states are compatible with the existence of concentration gradients. Therefore, let us now consider the axis-symmetric approximation of Figure 4.8a, *i.e.* the rotationally invariant surface of Figure 4.8c.

Equilibria are found as the stationary solutions of the Allen-Cahn equation with conserved global order parameter (see *e.g.* Rubinstein *et al.*[168]), namely:

$$\partial_t \phi = -\frac{\delta G}{\delta \phi} = D\nabla^2\phi - f'(\phi) - k'(\phi)H^2 - \bar{k}'(\phi)K + \mu \, , \tag{4.59}$$

where $\phi = \phi(\boldsymbol{r}, t)$ is now a function of both space and flow parameter t. We solve this equation using a finite difference method on unstructured triangular meshes. Meshes are constructed using the software package Gmsh[190]. We stress that the L^2-gradient flow generated by Equation 4.59 is purely fictitious and does not reflect the actual coarsening dynamics the binary fluid. However, this approach offers a practical way to generate stable equilibrium configurations for arbitrary geometries. Our main numerical results are shown in Figure 4.12a. We focus on the linear couplings that explicitly break the $\phi \to 1 - \phi$ symmetry of the free energy, since they offer the most interesting phenomenology. In all the simulations summarised in Figure 4.12, we set the temperature to $T = 0.9T_c$ with $T_c = qJ/2$ uniform over all S. As a guide to the eye, the numerical data are superimposed to the stable branch of the lines of equilibrium associated with the two disconnected spheres (see also Figure 4.9b), with $L_k + L_{\bar{k}} = 1/40\, qJR_1^2$. This value is almost an order of magnitude lower than the one used to construct the phase diagram of Figure 4.10b, yet it can be shown that it retains antimixed states as equilibrium solutions. Each data point is obtained upon averaging the numerically found stationary solutions of Equation 4.59 over ten random initial field configurations. To facilitate the comparison, the Φ_a values are computed by integrating ϕ over axisymmetric regions which have the same area fraction φ_1 as the one occupied by S_1 in the case of the two disjoint spheres. The solid horizontal (vertical) lines correspond to the Maxwell values $\phi_\pm$ on the small (large)

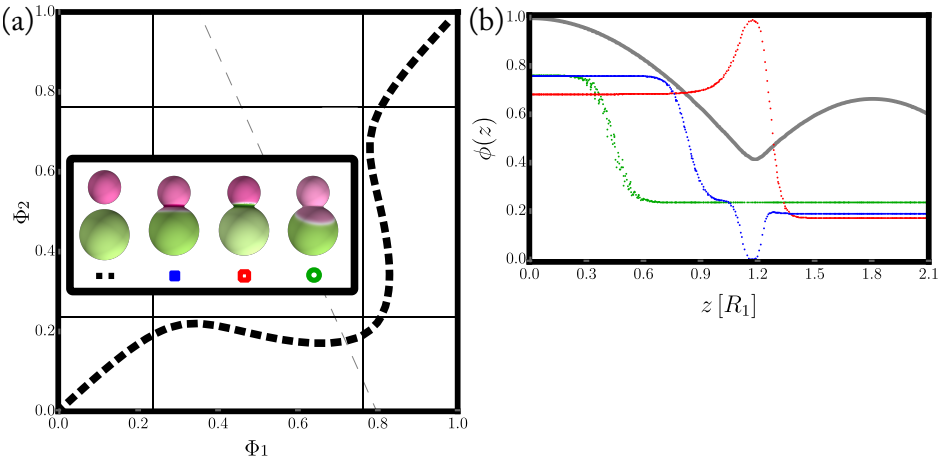

Figure 4.12: Equilibrium states of the axis-symmetric geometry of Figure 4.8c, obtained from numerical solutions of Equation 4.59 with mean-field potentials from 4.47 at sub-critical temperature $T = 0.45\,qJ$. **(a)** Lines of equilibrium for different $L-$couplings: the solid blue squares have $L_k = 1/40\,qJR_1^2$, the empty red squares have $L_{\bar{k}} = 1/40\,qJR_1^2$ and the empty green circles have no direct interactions. The dashed black line is the line of equilibrium obtained as in Figure 4.9 for the two-spheres geometry with $L_k + L_{\bar{k}} = 1/40\,qJR_1^2$. The solid vertical and horizontal lines are the binodal concentrations $\phi_\pm$ at zero coupling. The inset shows what the four different equilibria look like at the same total concentration $\Phi = 0.55$ (shown as a dashed gray line in the main plot). **(b)** Concentration profiles as function of the arc-length axis-symmetric coordinate z, for the three dumbbells shown in the inset of (a). The thin black line in the background shows the radial profile of the surface (in cylindrical arc-length coordinates, the profile of a sphere looks like a trigonometric sine). The two horizontal dashed lines correspond to the Maxwell values $\phi_\pm$. In all simulations we set $\epsilon = 0.024\,R_1$.

sphere. In general, if the local concentrations take the binodal values, $\Phi_a = \phi_\pm$, it means that the system is likely phase separated, with the interface lying in only one sub-region of S.

The differently colours denote different values of L_k and/or $L_{\bar{k}}$, while keeping the $Q-$couplings to zero. Different data points with the same colour correspond to different values of Φ. The green circles corresponds to the homogeneous case, where also $L_{k,\bar{k}} = 0$, and demixing occurs uniformly over the entire surface. Outside of the binodal interval, *i.e.* for either $\Phi < \phi_-$ or $\Phi > \phi_+$, the equilibrium state is homogeneously mixed with $\Phi_1 = \Phi_2 = \Phi$ and the data points are aligned along the diagonal. Conversely, phase separation occurs when $\phi_- \leq \Phi \leq \phi_+$, for which the data points depart from the diagonal and either Φ_1 or Φ_2 - the one containing no interfaces - coincide with $\phi_\pm$.

The square dots correspond to either L_k (full blue) or $L_{\bar{k}}$ (empty red) equal to $1/40\,qJR_1^2$, with all other couplings set to zero. In both cases we find that the numerical results follow qualitatively the dashed line of equilibrium. The coupling with the squared

mean curvature, L_k, seems to be the one that follows the two disjoint sphere results more closely, and is the only one of the two data sets that features configurations with $\Phi_1 > \phi_+$ and $\Phi_2 < \phi_-$ (see the bottom-right corner of Fig. 4.12a).

Interestingly, for some Φ, the equilibrium concentrations depart from a line of equilibrium and follow the horizontal (or vertical) binodal line, although only in a specific range of parameters (*e.g.* red dots, with $\Phi < 0.5$) the data exhibit ϕ values that approximate the binodal value ϕ_- with reasonable accuracy. In all other cases, Φ_a relaxes toward different Φ-independent values. This behaviour likely originates from one or both of the following features of our model. First, the interpretation of Φ_a is less stringent when applied to a connected dumbbell, where the two lobes are not geometrically distinct regions. Second, there might be additional contributions resulting from the finite thickness of the interface ($\epsilon = 0.024R_1$ in Figure 4.12). In general, these observation indicate that, in non-homogeneous spaces, the definition itself of phase-separation requires special care.

This latter statement can be made more precise by considering the inset of Figure 4.12a and Figure 4.12b. In both plots, $\Phi = 0.55$, corresponding to the dashed diagonal line in Figure 4.12a. This value lies within the miscibility gap, thus, in the absence of an explicit coupling with the curvature, the system phase separates, and since $\Phi \neq \varphi_a$, the expected areas occupied by the two phases do not match the relative size of the two lobes, so that the interface will lie away from the neck of the dumbbell. The snapshots in the inset of Figure 4.12a are colour-coded based on the local ϕ value, with $\phi = 0$ in magenta, $\phi = 1$ in green and $\phi = 1/2$ in white. The rightmost snapshot illustrates the case of homogeneous phase-separation with the associated interface lying along a constant geodesic curvature line, as predicted by Equation 4.38 for homogeneous potentials.

Figure 4.12b shows a plot of ϕ along a meridian as a function of the arc-length z from the equator of the larger sphere. The green dots show the interfacial profile of the classical phase-separated configuration, *i.e* the hyperbolic tangent kink interpolating between ϕ_+ and ϕ_-. The dots are not perfectly aligned since the interface itself is not axisymmetric, so the arc-length z does not match exactly the geodesic normal coordinate. When either L_k (blue dots) or $L_{\bar{k}}$ (red dots) are switched on, the configuration of the phase field ϕ changes dramatically. The field now interpolates between values which are *not* the binodal values - shown as two horizontal dashed lines in the plot - a signature of the fact that the curvature affects the bulk concentration, even away from high curvature regions. The influence of the curvature becomes particularly striking in the neck region, where the Gaussian and mean curvature couplings give rise to opposite effects. Since H^2 is always positive, the coupling $L_k\phi H^2 > 0$ favours small ϕ values in regions of high curvature, as demonstrated by the prevalence of magenta tones around the neck. Conversely, since $K < 0$, the coupling $L_{\bar{k}}\phi K$ is negative and favours higher ϕ values, as indicated by the prevalence of green tones. This behaviour is reversed in case $L_{\bar{k}} < 0$, but, given the arbitrariness in the definition of the field ϕ, this does not change the qualitative picture.

Notice that in both cases the interface is slightly shifted away from the neck, a phenomenon which is reminiscent of the behaviour of phase domains in axisymmetric sharp interface models of free-standing lipid membranes[65]. Interestingly, both the blue

and green profiles are not monotonic functions of z. Finally, note that all three cases interpolate between different values in the two bulk regions: this proves that, in general, the distinction between inhomogeneous mixing and demixing is not well-defined: we choose to interpret the blue curve as the realisation of the antimixed state (since the profile interpolates between values which are outside the local miscibility gap) on a single, connected, smooth geometry.

4.4 Conclusions

In this chapter, we reported a theoretical investigation of the equilibrium configurations of binary lipid mixtures on curved substrates. The difference in stiffness between the two lipid phases introduces a coupling mechanism between the chemical composition of the lipids and substrate curvature, whose primary effect is to pin the stiffer phase in regions of low curvature, at the expense of the softer phase[4;18]. When the bending energy difference is sufficiently large to overcome interfacial tension, this mechanism might lead to the formation of multiple finite domains of one phase. However, the existence of multiple domains alone does not imply a direct coupling between composition and curvature, as interfaces on a curved surface can be simultaneously curved and length-minimising.

In Section 4.2, we have highlighted with special care the role of the area fraction φ (*i.e.* the percentage of the total available area covered by either one of the two phases) and demonstrated how this dramatically affects interfacial stability. Upon minimising the Cahnham-Helfrich free energy on a generic curved surface, we derived a curved-space analogue of the Young-Laplace law from which we could identify three fundamental scenarios. In the absence of direct coupling with curvature, interfaces lie along geodesics (for non-conserved area fraction), or lines of constant geodesic curvature (for conserved area fraction). A direct coupling with curvature introduces an additional, space-dependent, Laplace pressure at the interface, proportional to the difference between the bending moduli and to the local mean squared and Gaussian curvatures. This causes the interface to deviate from the local geodesics and to become more and more curved the larger the difference in stiffness between the two phases is. In all these cases, negative Gaussian curvature enhances the stability of the interface, since deviations from minimal shapes are necessarily penalised.

We have then restricted our analysis to specific classes of surfaces of both practical and conceptual interest. In the case of spherical substrates, we showed that, for non-conserved area fractions, interfaces are always unstable and equilibrium is achieved upon expelling the stiffer phase from the spherical substrate. For conserved area fractions, on the other hand, a stable equilibrium configuration consists of a single circular interface, regardless of the difference in the bending moduli. We considered axis-symmetric surfaces, whose geometry is completely determined by the shape of an axial cross-section. Thanks to their simplicity, this class of surfaces has played a special role in literature[65;191–193] and represents the only case where analytical progress can be made even in the general problem, where both the shape of the membrane and geometry of the interfaces are allowed to change. Furthermore, axis-symmetric membranes have been experimentally investigated,

both in the context of giant unilamellar vesicles[4;66] and colloid supported lipid bilayers in this thesis. We mapped out a complete phase diagram in terms of the area fraction φ and dimensionless number η_k and $\eta_{\bar{k}}$ expressing the relative contribution of bending and interfacial tension to the total energy.

In Section 4.3, we investigated the thermodynamic equilibrium of two-dimensional fluids confined on closed spatially curved substrates. We considered a binary mixture that can be characterised by a single scalar order parameter ϕ. Crucially, we focused on closed thermodynamical systems, *i.e.* systems where there is no exchange of ϕ with the surrounding environment. This implies that the average total concentration, Φ, is an externally fixed parameter. Equilibrium states are found from minimisation of the Gibbs free energy $G = F - \hat{\mu}\Phi$, where the chemical potential $\hat{\mu}$ here is set by the constraint on the total concentration.

We constructed the most general form of F, using only symmetry and scaling arguments, and identified four $\phi-$dependent parameters that, together with the total concentration Φ, determines the equilibrium state of the system. These are: the compressibility D, the homogeneous free energy density f and the two bending moduli k and $\bar{k}$. We reviewed the classical theory of phase separation for coexisting liquids. We reviewed the boundary layer analysis of the thin interface limit of two-dimensional phase-field models on curved surfaces, without direct curvature interactions. We used a mean-field approximation of a microscopic lattice-gas model with curvature dependent interactions. By using this model, we found that the curvature of the substrate directly affects the structure of the free energy landscape via four non-equivalent couplings, which either break or preserve the symmetry of the free energy under exchange of the two phases (*i.e.* $\phi \to 1 - \phi$). We refer to them respectively as $Q-$ and $L-$interactions.

Motivated by the experimental results in Chapter 3, we applied our model to dumbbell-shaped membranes, as shown in Figure 4.8. For simplicity, we first approximated this surface as consisting of two disjointed spheres, allowed to exchange order parameter, but otherwise isolated from the environment. We found that $L-$interactions, which linearly couple with the order parameter ϕ, favour states with non-zero $\Delta\Phi$ (see Equation 4.52), *i.e.* a single phase with non-uniform concentration across the system. For our simple two-sphere geometry, this implies that each sphere is characterised by a distinct ϕ value, depending upon the strength of the $Q-$ and $L-$couplings and the local curvature radius.

For certain specific Φ values, such a state remains stable even below the critical temperature. In this regime, the inhomogeneity becomes more severe and the two spheres exhibit a stark concentration difference, even though phase separation has not occurred. This state observed in Chapter 3 is named antimixed state to stress that, albeit still in the mixed phase, the equilibrium concentrations split on the antipodes, or opposite sides, of a local miscibility gap. Surprisingly, this behaviour depends on the linear couplings between the concentration and the local curvature (*i.e.* the $L-$coupling, in our notation), despite these not altering the Maxwell construction and being thermodynamically irrelevant in binary membranes confined on homogeneous substrates. This originates from the fact that, in the presence of sufficiently large geometrical inhomogeneities and sufficiently strong symmetry-breaking coupling with curvature, the phase diagram partitions into two

sub-diagrams, each with its own distinct critical point.

Lastly, we verified that antimixing persist also on more realistic dumbbell-shaped substrates, obtained by connecting two spherical caps with a smooth neck. In this case, inhomogeneous mixing demands the occurrence of sharp concentration gradients, whose structure is substantially different than that of standard interfacial profiles. Most importantly, the average concentrations on the spherical lobes, *i.e.* the regions away from the neck, differ from the binodal values, even if the thermodynamic potential has the same Maxwell concentrations everywhere.

Acknowledgements

I am very grateful to the collaboration with Piermarco Fonda, who has developed and performed all the analytical calculations and numerical simulations presented here.